AIP | Review of Scientific Instruments

Indentation device for in situ Raman spectroscopic and optical studies

Y. B. Gerbig, C. A. Michaels, A. M. Forster, J. W. Hettenhouser, W. E. Byrd et al.

Citation: Rev. Sci. Instrum. **83**, 125106 (2012); doi: 10.1063/1.4769995
View online: http://dx.doi.org/10.1063/1.4769995
View Table of Contents: http://rsi.aip.org/resource/1/RSINAK/v83/i12
Published by the American Institute of Physics.

Indentation device for *in situ* Raman spectroscopic and optical studies

Y. B. Gerbig,[1,a)] C. A. Michaels,[2] A. M. Forster,[3] J. W. Hettenhouser,[3] W. E. Byrd,[3] D. J. Morris,[1,b)] and R. F. Cook[1]
[1]*Ceramics Division, National Institute of Standards and Technology (NIST), Gaithersburg, Maryland 20899, USA*
[2]*Surface and Microanalysis Science Division, NIST, Gaithersburg, Maryland 20899, USA*
[3]*Materials and Structural Systems Division, NIST, Gaithersburg, Maryland 20899, USA*

(Received 28 August 2012; accepted 19 November 2012; published online 12 December 2012)

Instrumented indentation is a widely used technique to study the mechanical behavior of materials at small length scales. Mechanical tests of bulk materials, microscopic, and spectroscopic studies may be conducted to complement indentation and enable the determination of the kinetics and physics involved in the mechanical deformation of materials at the crystallographic and molecular level, e.g., strain build-up in crystal lattices, phase transformations, and changes in crystallinity or orientation. However, many of these phenomena occurring during indentation can only be observed in their entirety and analyzed in depth under *in situ* conditions. This paper describes the design, calibration, and operation of an indentation device that is coupled with a Raman microscope to conduct *in situ* spectroscopic and optical analysis of mechanically deformed regions of Raman-active, transparent bulk material, thin films or fibers under contact loading. The capabilities of the presented device are demonstrated by *in situ* studies of the indentation-induced phase transformations of Si thin films and modifications of molecular conformations in high density polyethylene films. [http://dx.doi.org/10.1063/1.4769995]

I. INTRODUCTION

Instrumented indentation—in which the indentation load and indenter displacement are measured during the contact event—is a widely used technique for fundamental studies of materials physics as well as for evaluative analyses of the mechanical properties and performance of materials and structures in specified engineering,[1] biological, or biomedical applications.[2] Although the mechanical behavior of materials can be assessed quantitatively in conventional instrumented indentation tests, the fundamental mechanisms responsible for such behavior are seldom observed directly.[3] In conventional instrumented indentation tests, it is only possible to characterize modifications in the material or to the material stress state on residual indentation artifacts, often leaving scientists with more speculations than measurable facts to describe the kinetic and physical processes occurring during the indentation event. To overcome this problem, the indentation technique has been augmented with various *in situ* capabilities, such as optical microscopy,[4–10] acoustic measurements,[11] scanning electron microscopy,[12] transmission electron microscopy,[13,14] X-ray diffraction,[15] contact resistance measurements,[16–19] or Raman spectroscopy.[20,21]

Raman spectroscopy—in which small changes in the frequency of light are measured during scattering events—has become a versatile tool for characterizing the molecular structure, orientation, and stress state of materials at the micro- and nano-scales. Raman analysis is commonly employed to investigate pressure-induced phenomena such as phase transitions[20,22] or ferroelastic domain switching.[23] From the Raman spectra of polymers, information can be obtained about the effect of pressure on, for example, crystallinity,[24] molecular orientation of the polymer chains,[25] or coupling between vibrational modes of crystalline and amorphous segments.[26,27]

Raman spectroscopy is widely used to determine residual stress distributions in ceramic[28,29] and semiconductor materials.[30–32]

The utility of instrumented indentation and Raman spectroscopy has led several researchers to explore combinations of the methods for *in situ* measurements. In the *in situ* Raman experiments presented by Jochum *et al.*[20] a polygonal, flat diamond punch was connected to a Raman microscope for analysis of the indented region. As the analyzing beam is required to focus through the indenting tip (the punch), the tip geometry and tip material limit the application range. The microindentation device for *in situ* Raman analysis developed by Gogotsi *et al.* has an adaptable design that allows focusing of the laser beam for Raman analysis through the sample parallel, perpendicular, or at an angle of 45° to the indentation axis.[21] However, this device lacks an accurate displacement measurement which hinders the collection of force-displacement curves essential for the evaluation of the strain dependent behavior of materials through indentation.

This current work describes the design, calibration, and operation of an indentation device with *in situ* Raman spectroscopy and optical microscopy capabilities, and which allows the collection of force-displacement data in parameter ranges comparable to commercial instruments. The capabilities of the presented experimental setup are demonstrated by *in situ* studies of the indentation-induced phase

a)Author to whom correspondence should be addressed. Electronic mail: yvonne.gerbig@nist.gov.
b)Present address: Michelin Americas Research and Development, Greenville, South Carolina 29605, USA.

transformations of Si thin films and modifications of molecular confinement in high density polyethylene (PE) films.

II. INDENTATION DEVICE

A. Design of the indentation device

A three-dimensional rendering and schematic cross-sectional diagram of the indentation device are shown in Fig. 1. The central element of the device is a linear solenoid actuator (LSA) consisting of a solenoid housing containing a fixed permanent magnet and a moving coil (NCC03-15-050-2X, H2W Technology Inc., Santa Clarita, CA).[33] The LSA provides the indentation force up to maximum of 5 N. The LSA housing is mounted to an upper fixed solenoid plate that is attached to a metal frame composed of two spacer legs mounted on a bottom plate. The moving LSA coil is suspended by two ortho-planar linear-motion springs made of copper-beryllium sheet metal. This special spring design ensures the linearity and repeatability of the movement[34] of the suspended LSA coil. The springs are exchangeable such that varying the thickness of the springs modifies the stiffness of the system. The springs themselves are mounted between fixed spring clamp plates attached to the frame and secured by spring clamp nuts.

A thread mount to hold an indenter tip is attached to the lower spring assembly. The device utilizes indentation tips of commonly used as well as custom-made geometries (e.g.,

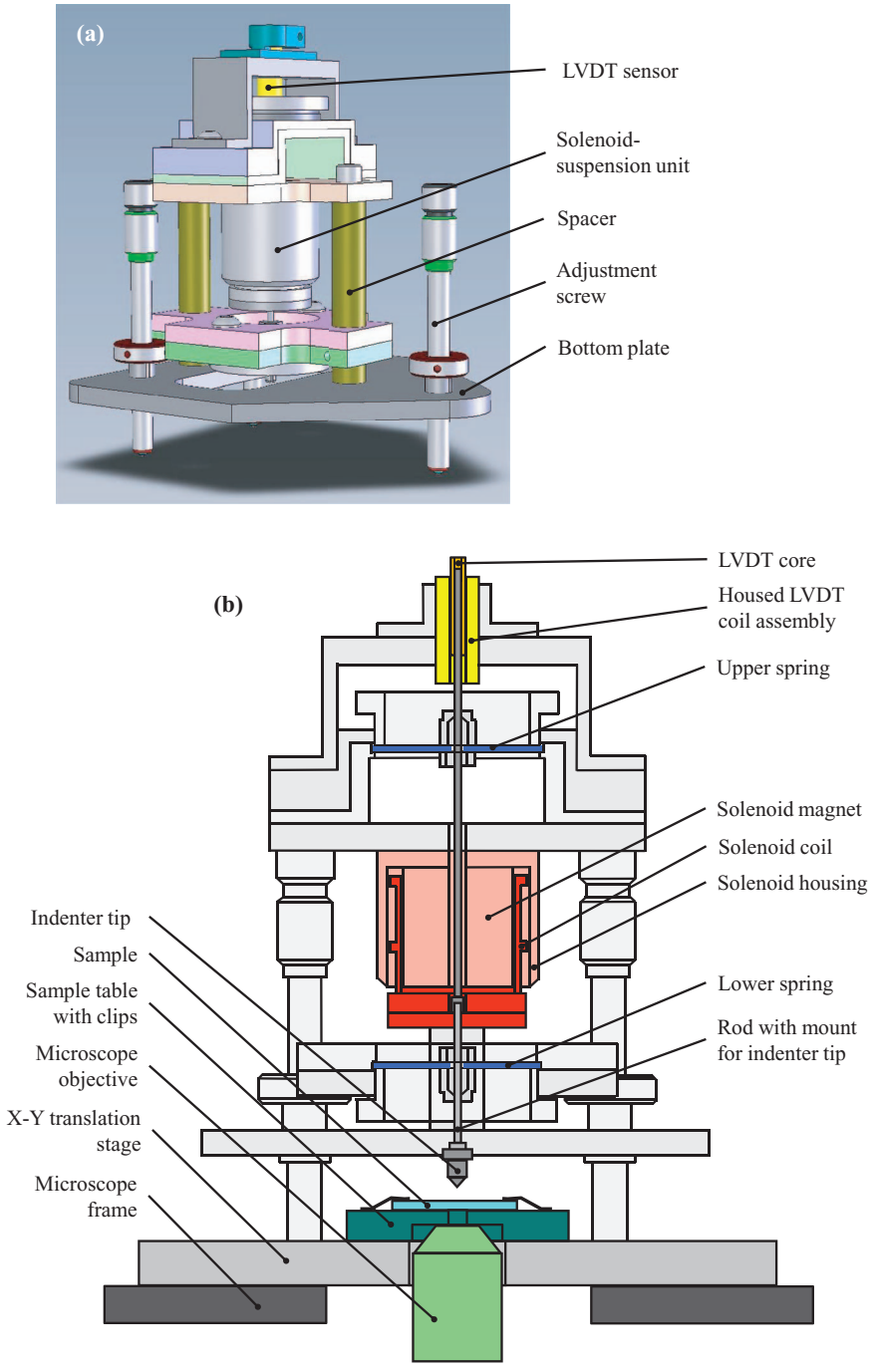

FIG. 1. Design and components of instrumented indention device in (a) side view and (b) cross sectional view, when installed in the Raman microscope.

Berkovich, cube corner, flat punch, and conospherical shape) and materials (e.g., diamond, sapphire, tungsten carbide, steel) making it possible to adapt the contact geometry to reproduce specific test conditions as necessary. A rod attached to the upper spring assembly is threaded to the moving core of a linear variable differential transformer (LVDT) sensor (CD 375-050, Macrosensor, NJ).[33] The LVDT measures the indenter tip displacement (detection range is 1 mm).

The spacer columns hold the force transducer and the displacement sensor orthogonal to the base plate. Also attached to the base plate are three adjustment screws that are used for manual, coarse positioning of the indenter tip in the vertical direction. When installing the indentation device in the Raman microscope, the adjustment screws are slipped into kinematic-coupling notches in the *X-Y* translation stage of the microscope. The vertical axis of the indentation device is, thereby, automatically positioned close to the optical axis of the microscope. Micrometer screws attached to the microscope *X-Y* translation stage are used to align the indentation device and a sample table with the optical axis of the microscope objective and, thus, realize fine alignment (± 1 μm) between indenter axis and optical axis. The sample table is magnetically mounted to the *X-Y* translation stage using rare earth magnets and has an aperture in the center that allows the Raman excitation laser beam to be focused through the specimen into the sample region in contact with the indenter tip. The sample is clamped onto the sample table with clips (PELCO SEMClip™, Ted Pella, Inc., Redding, CA)[33] for easy sample mounting and exchange.

B. Operation of the indentation device

The indentation device works according to the following principle: The incorporated LSA uses a permanent magnetic field and a conducting coil winding to produce an electromagnetic force proportional to the current passing through the coil according to the Lorentz force principle. When the indenter tip is hanging in air, the electromagnetic force generated by the LSA is opposed by the mechanical restoring force of the suspension springs. (The gravitational force is considered constant and its influence is considered negligible.) If the electromagnetic force is unequal to the spring force, the coil of the LSA moves, driving the attached indenter tip in the same direction as the LSA. By varying the coil current, the coil with the tip can be moved towards or away from the sample surface. When the indenter tip is in contact with the sample, LSA motion is opposed by both the suspension springs and the indentation contact force; a defined force can be applied to the sample surface by manipulating the coil current. The LSA is controlled via a linear power amplifier (SMA5005, Glentek, In., El Segundo, CA)[33] in an open loop mode. The linear power amplifier converts a signal voltage coming from the control and data acquisition (DAQ) system to a drive current to actuate the LSA. By varying the rate of change and magnitude of the signal voltage, the maximum force as well as loading and unloading rates can be modified during the indentation test. The drive current signal from the linear power amplifier is conveyed back to the DAQ system and recorded to determine the force.

The displacement of the LSA coil and thus the attached indenter tip is measured using the LVDT sensor. A LVDT is a variable transformer that converts the rectilinear motion of an object to which it is mechanically coupled into a proportional electrical signal. The sensor consists of a stationary coil assembly and a separate core that is free to move axially within the hollow bore of the coil assembly. In operation, the primary winding of the coil is energized by constant alternating current. The resulting magnetic flux is coupled by the core to the adjacent secondary windings. The electrical output signal of the LVDT is the differential ac voltage between the two secondary coil windings, which varies with the axial position of the core within the coil assembly. In this application, the LVDT core was mechanically coupled by a rod to the coil of the LSA. A stabilized function generator (Wavetek 21 Stabilized Function Generator 11 MHz, Aeroflex, Ismaning, Germany)[33] supplies the excitation voltage to the primary coil of the LVDT sensor. A lock-in amplifier (SR830 DSP, Stanford Research Systems, Sunnyvale, CA)[33] determines the differential voltage between the voltage induced to secondary coils and the excitation voltage supplied by the waveform generator.

The raw data (drive current signal of the LSA and differential LVDT voltage) are simultaneously collected, processed, and converted to force and displacement values by the DAQ system enabling the recording of force-displacement curves during the indentation experiment. The conversion factors were determined for the specific configuration of the indentation device prior to the measurements, as described in Sec. II C.

C. Calibration and technical specifications of the indentation device

1. Displacement measurement

A conversion factor k_{dis} was determined to transform the change in measured LVDT voltage ΔV into a displacement value $\Delta h = k_{\mathrm{dis}} \Delta V$. For this purpose the LVDT sensor was installed in a calibration fixture, in which the core of the LVDT sensor was mechanically attached to a micrometer screw, enabling controlled displacement of the core. The change in the induced LVDT voltage was recorded as a function of the core displacement and fitted to a linear equation. The slope of the fitted line represents the conversion factor k_{dis}, which was determined to be 114.80 μm/V $\pm$ 0.8 μm/V (Type A uncertainty, $k = 1$, five repeated measurements).[35]

2. Force measurement

The net force F applied to the sample surface by the indenter tip is the difference between the electromagnetic force F_{em} generated by the LSA and the counteracting spring force F_{sp} of the suspension system. Thus, the applied indentation force is given by

$$F = F_{\mathrm{em}} - F_{\mathrm{sp}} = i_{\mathrm{s}} \times k_{\mathrm{s}} - h \times k_{\mathrm{sp}}, \quad (1)$$

where i_{s} is the signal current measured at the LSA amplifier, k_{s} is the solenoid constant (k_{s} is equal to the product of the magnetic field strength and conductor length, both constants

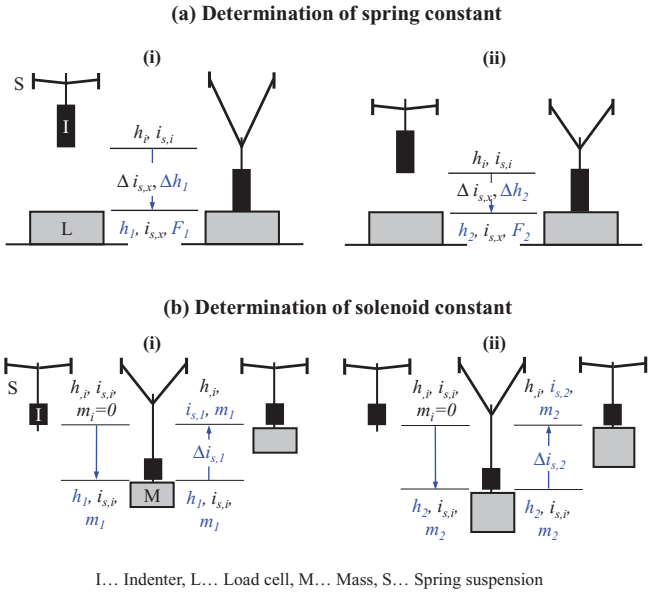

FIG. 2. Schematic diagrams of the calibration procedures for determining (a) the spring constant k_{sp} and (b) the solenoid constant k_s.

in this study), k_{sp} is the spring constant of the suspension system, and h is the deflection of the suspension springs.

In order to determine the indentation force, the solenoid constant k_s and the spring constant k_{sp} have to be measured. Sections II C 2 a and II C 2 b explain the procedure employed to determine those constants.

a. Determination of k_{sp}. A calibration of the spring constant required the indenter to push against a load cell at different signal currents. A flat punch (diameter 5 mm) was installed on the indenter to avoid damaging the load cell when pressing on it. The load cell readings were displayed by a connected control unit. The load cell (range 0 N to 1 N) was calibrated using standard masses from 1 g to 100 g. An initial signal current $i_{s,i}$ was input to the LSA to move the indenter tip to an initial location h_i (Fig. 2(a)). The tip position was measured using the LVDT sensor. The load cell was placed beneath and close to the indenter, but not touching. In order to push onto the load cell, the indenter was displaced by a distance Δh_1 by changing the signal current to a second value of $i_{s,x}$. The current was held constant at $i_{s,x}$ for a hold period, in which the force F_1 on the load cell was measured and verified constant within 1% of the average value. For the second test, the current was changed back to $i_{s,i}$ to place the indenter at location h_i and the indenter tip was moved closer to the load cell. When the same current $i_{s,x}$ as in the first test was applied, the indenter was displaced by the distance Δh_2 from its initial position and generated a force F_2 during the hold period. The forces F_1 and F_2, generated when the current $i_{s,x}$ was applied, were calculated according to Eq. (1):

$$F_1 = \Delta i_{s,x} \times k_s - \Delta h_1 \times k_{sp}, \tag{2a}$$

$$F_2 = \Delta i_{s,x} \times k_s - \Delta h_2 \times k_{sp}, \tag{2b}$$

with $\Delta h_1 = h_i - h_1$, $\Delta h_2 = h_i - h_2$ and $\Delta i_{s,x} = i_{s,i} - i_{s,x}$ (see Fig. 3(a)).

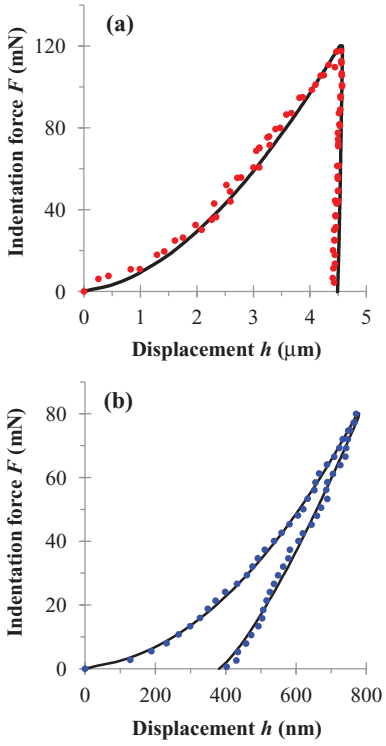

FIG. 3. Force-displacement curves recorded with the developed indentation device (dotted line) and a commercial indenter (solid line) during an indentation with Berkovich diamond tip on (a) aluminum and (b) fused silica samples.

By combining Eqs. (2a) and (2b), k_{sp} can be determined by

$$k_{sp} = \frac{F_1 - F_2}{\Delta h_2 - \Delta h_1}. \tag{3}$$

The spring constant k_{sp} was measured to be 191.3 N/m $\pm$ 1.3 N/m (Type A uncertainty, coverage factor $k = 1$ from five repeated measurements)[35] for the instrument configuration employed in the studies presented here. This is within the range typical of commercial instrumented indenters.

b. Determination of k_s. A calibration of the solenoid constant required the indenter to lift masses at different signal currents. A specially designed holder was installed onto the indenter for attaching the calibrated standard masses. At an initial signal current $i_{s,i}$, the indenter tip was placed at its initial location h_i (Fig. 2(b)). When a mass m_1 was attached to this indenter tip, it was displaced by the distance Δh_1. In order to retract the tip with the attached mass m_1 to the initial position, the signal current was changed to a value $i_{vc,1}$. In a second test, a mass m_2 was attached to the indenter tip leading to a displacement of the tip by Δh_2 from its initial position (under current $i_{s,i}$). The signal current was adjusted to a value $i_{vc,2}$ to return the tip with the attached mass m_2 to the same initial position h_i as in the first test. The forces F_1 and F_2 generated by the masses m_1 and m_2 at the tip were calculated according to Eq. (1):

$$F_1 = g \times m_1 = \Delta i_{vc,1} \times k_s - h_i \times k_{sp}, \tag{4a}$$

$$F_2 = g \times m_2 = \Delta i_{vc,2} \times k_s - h_i \times k_{sp}, \tag{4b}$$

where g is the gravitational acceleration constant ($g = 9.81$ m/s), $\Delta i_{vc,1} = i_{s,i} - i_{vc,1}$ and $\Delta i_{vc,2} = i_{s,i} - i_{vc,2}$ (see Fig. 2(b)). By combining Eq. (4a) in Eq. (4b), k_s can be determined by

$$k_s = \frac{g \times (m_1 - m_2)}{\Delta i_{vc,1} - \Delta i_{vc,2}}. \quad (5)$$

The solenoid constant k_s was determined to be 982 mN/mA ± 12 mN/mA (Type A uncertainty, $k = 1$, five repeated measurements).[35]

3. Frame compliance

The frame compliance (important for the measurement of accurate force–displacement curves) has been determined based on the Oliver and Pharr method[36] by a series of indentations on fused silica and sapphire references. A frame compliance C_f of 1.6 nm/mN ± 0.1 nm/mN (Type A uncertainty, $k = 1$, at least five measurements per material)[35] was determined; this is comparable to commercial instruments. A frame displacement of $C_f P$ was subtracted from the LVDT displacement data for all measurements, where P is the instantaneous indentation force. The force-displacement data recorded by the designed device are in good agreement with data obtained by commercial indentation instruments (Fig. 3).

4. Resolution of force and displacement measurement

In order to evaluate the resolution of the force and displacement measurements, the noise in the corresponding signals was determined by sending a constant signal voltage to the LSA amplifier for a fixed time and calculating the deviation in the force and displacement signals during this period. The standard deviation around the average value was 1.5 mN for the force and 35 nm for the displacement signals. These values are taken as the instrumental resolution for the force and displacement values measured with this device in its current configuration.

III. RAMAN MICROSCOPE

The indenter was placed on the sample stage of a commercial inverted optical microscope (IX-71, Olympus, Center Valley, PA);[33] this arrangement allowed for the examination of the indenter probe and sample using conventional bright field, reflected white light imaging, and, after switching to a laser port for beam entry into the light path, Raman microspectroscopy of the sample. The optical portion of the instrument is illustrated schematically in Figure 4. The following description of the instrument microscopy capabilities will be split into several parts; each describing modular aspects of the overall optical design.

A. White light imaging

Optical imaging of the sample and indenter probe is performed using the traditional imaging path of the inverted microscope. The light source is a collimated light emitting diode (LEDC17, Thorlabs, Newton, NJ)[33] chosen to eliminate increases in the air temperature within the microscope enclosure observed during use of a halogen source. The light reflects from a brightfield mirror unit (U-MBF3, Olympus, Center Valley, PA),[33] mounted within a six unit mirror turret, into the objective. Two ultra long working distance (ULWD) metallurgical objectives are used for white light imaging; a 50×, 0.55 NA or an 80×, 0.75 NA objective (Olympus, Center Valley, PA).[33] The sample table and substrate thicknesses set a minimum value required for the working distance and necessitate the use of ULWD objectives. The reflected light passes through the collection path into either an eyepiece or to a camera port equipped with a color charge coupled device (CCD) camera (XCD-U100CR, Sony, Park Ridge, NJ)[33] for image storage. It is worth noting explicitly that this configuration requires the use of samples that are nominally transmissive in the visible and near-IR spectral region.

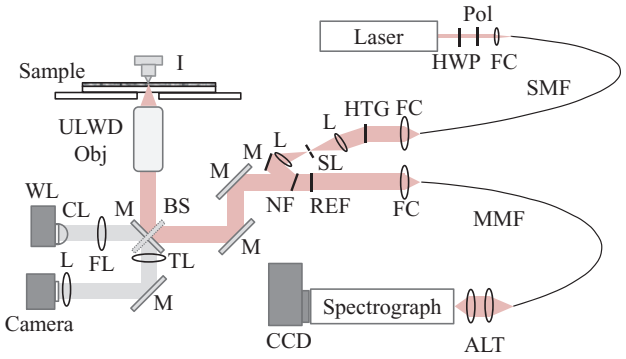

ALT … achromatic lens telescope, BS … beam splitter, CCD … charge couple device, CL … collecting lens, FC … fiber coupler, FL … field lens, HTG … holographic transmission grating, HWP … half-wave plate, I … indenter, L … lens, M … mirror, MMF … multimode fiber, NF … notch filter, Pol … polarizer, REF … Raman edge filter, SL … slit, SMF … single-mode fiber, TL … tube lens, YULWD Obj … ultra long working distance objective, WL … white light source

FIG. 4. Schematic diagram of the optical portion of the instrument used for white light imaging and Raman microprobing.

B. Laser

The light source used for Raman spectroscopy is a continuous wave, 785 nm diode laser (785 XM, Torsana, Solna, Sweden)[33] with nominal output power of 500 mW. The laser output passes through a combination of a half waveplate and polarizer that serves as a variable attenuator prior to coupling into a single mode optical fiber (mode field diameter of 5.6 μm) for spatial filtering and transport to the microscope enclosure. Typical laser powers incident on the sample are generally in the 2 mW to 20 mW range; see text below for specific values.

C. Raman microscope

Light exiting the transport fiber is collimated, passed through a polarizer, and then diffracted from a holographic transmission grating into a spatial filter consisting of a lens, slit, and a second lens. The slit is positioned to clean up the

laser spectrum by passing the 785 nm beam while blocking Raman scattered light originating from the transport fiber glass. This arrangement insures that the bandwidth of the excitation beam is much smaller than the spectrograph resolution and thus is not the factor limiting the attainable spectral resolution. The beam then reflects from a holographic notch filter (Kaiser Optical Systems, Ann Arbor, MI)[33] into the laser port of the microscope where it is directed into the objective by a filter that is highly reflective in the 700 nm to 1000 nm band while also highly transmissive in the visible. Note that this filter occupies a different slot in the six unit mirror turret than the brightfield mirror; Raman and white light imaging using the LED illumination source cannot be performed simultaneously. However, the filter was chosen such that imaging with external oblique angle illumination of the indenter probe and sample will produce images in the eyepiece or the camera. Additionally, a small fraction ($\sim$1/100) of the 785 nm light reflecting from the sample will pass through the filter revealing the position of the Raman excitation beam with respect to features on the sample and the indenter probe. This arrangement is critical for co-locating the tip, sample, and excitation beam such that the collected Raman spectra arise from the sample region in contact with the indenter tip.

The aforementioned ultra long working distance metallurgical objectives are used to illuminate the sample and collect the Raman scattering. The focal lengths of these objectives are 8.1 mm (50×) and 4.1 mm (80×). The diffraction limited beam diameters that are attainable with these objectives at this wavelength are nominally 1.7 μm (50×) and 1.3 μm (80×). The diffraction limited depth of field for these two objectives at the excitation wavelength are nominally 10.4 μm (50×) and 5.6 μm (80×). However, the focal volume is undoubtedly larger than suggested by these values as the beam is focused through a substrate of some non-trivial thickness. Clearly the substrates possess indices of refraction greater than one; this is obviously not the design scenario for metallurgical objectives and one in which both the lateral and depth resolution is degraded from the diffraction limited case. Nevertheless, the degraded spatial resolution compared to the diffraction limited case is a necessary compromise to allow for meaningful mechanical testing. The actual spatial resolution attained is sample dependent, depending on the refractive index and thickness of the substrate and sample; quantitative measures of this resolution require Raman mapping capability. This instrument is currently only capable of microspectroscopy, but an upgrade to include mapping via laser scanning is in the planning stages. Despite not achieving diffraction-limited lateral resolution, the lateral spatial resolution for the samples reported here is expected to be significantly smaller than the radius of curvature ($>$10 μm) of any of the indenter probes utilized.

The scattered Raman light follows the illumination path back to the notch filter through which it passes onto a subsequent Raman edge filter (Semrock, Rochester, NY)[33] that provides further attenuation at the excitation wavelength. The Raman scattered light then passes through a polarizer and is coupled into a 50 μm core diameter multimode optical fiber for transport to the spectrometer. An 805 nm diode laser can be coupled into the collection fiber in reverse to allow visualization of the fiber core image in the microscope focal plane for the purpose of insuring optimal microscope alignment.

D. Spectrograph

The Raman light exiting the fiber is collimated and refocused with a telescope, consisting of two achromatic lenses, into a 250 mm focal length Czerny-Turner spectrograph (Chromex, Billerica, MA)[33] equipped with a 600 grooves/mm diffraction grating with a blaze wavelength of 750 nm. The telescope adjusts the cone angle of the light exiting the fiber to match to the *f*# of the spectrometer. A 1320 pixel × 400 pixel, back-illumination, deep depletion, liquid N_2 cooled CCD camera (Princeton Instruments, Trenton, NJ)[33] is placed at the output focal plane of the spectrograph. The mapping from CCD camera pixel number to Raman shift was calibrated using the known Raman line shifts for an acetaminophen test sample and a relative intensity correction for the Raman spectra was generated using a spectrum from a glass with a known luminescence spectrum, NIST Standard Reference Material (SRM™) 2241. The spectral resolution achieved with this setup is nominally 6 cm^{-1}.

IV. APPLICATION IN EXPERIMENTAL STUDIES

A. Mechanically induced phase transformation in silicon thin films

Silicon (Si) can be transformed to different crystallographic phases through mechanical stress[22,37] with far reaching consequences to its material properties influencing the performance of Si based micromechanical devices and structures.[17,38–40] In conventional indentation experiments, the exact path of Si phase transformation cannot be determined due to the sequential nature of the transformation process. *In situ* electrical resistance measurements between a conductive probe tip and the indented Si surface can allow indirect observations of phase transformation, as the conductivity of different Si phases may vary.[16,17,19,48] The unambiguous identification of phases is still very difficult with this method, as multiple phases can coexist in the transformation region.

In order to directly analyze indentation-induced Si phase transformations, a probing technique able to identify the crystallographic structure of phases must be employed. The developed device provides a promising experimental set-up for conducting *in situ* studies on pressure-induced phase transformations by coupling indentation with *in situ* Raman microscopy. An experiment was conducted with the device, in which a 600 nm thin Si film deposited on a sapphire substrate was indented with a conospherical diamond tip (nominal tip curvature radius 50 μm). The indentation force, and thus the contact pressure, was changed stepwise throughout the indentation experiment, whereby a Raman spectrum was collected at each step from the deformed contact region underneath the indenter. A more detailed description of the experimental procedure and evaluation of the data can be found in Gerbig *et al.*[49]

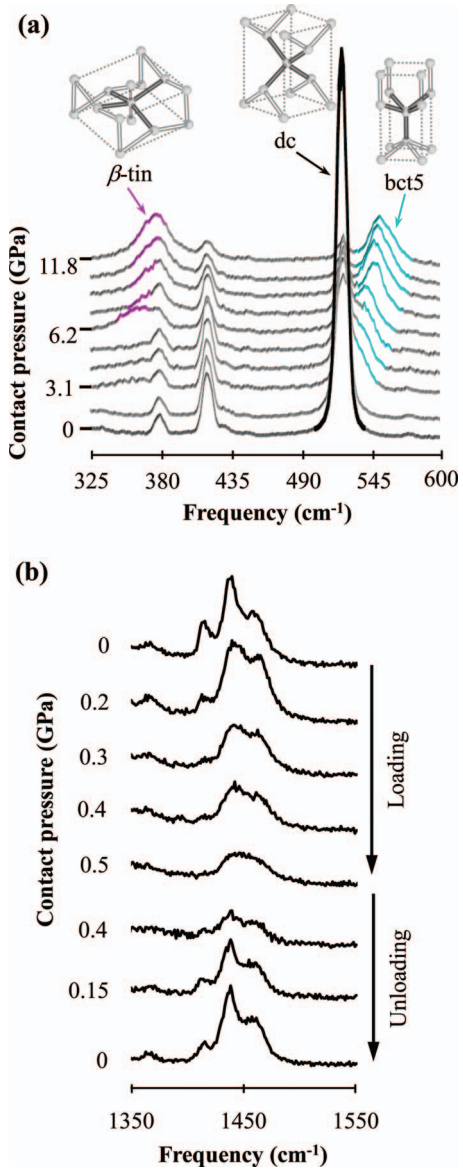

FIG. 5. (a) *In situ* Raman analysis of the indentation induced phase transformation in Si thin films with Raman spectra collected at different contact pressure during the loading segment of an indentation on the silicon thin film. The ball-stick models illustrate the crystallographic structure of the initial dc phase and the transformed Si structures (β-tin, bct5). (b) *In situ* Raman analysis of modification of the crystal structure of HDPE films during compression tests with Raman spectra collected on the indented HDPE film for different pressures.

As observed in the Raman spectra (Fig. 5(a)), the initial diamond cubic (dc) Si phase transformed gradually to β-tin during loading, confirming previous assumptions.[19,22,48] Simultaneously, the formation of an additional phase, which was identified as bct-5, was observed. Simulations of indentation experiments suggest that the dc crystal lattice of Si transforms into various body-centered tetragonal (bct) structures with both sixfold (β-tin) and fivefold coordination (bct5) during loading due to indentation-induced shear stresses.[41–47] The *in situ* study presented here provides experimental evidence for both the existence of this phase and the possibility of generating it under indentation conditions.

In situ experiments conducted with the presented device provide new insights on the transformation processes in Si during indentation, as it was possible to directly observe the onset of its primary phase transformation. This emphasizes the relevance and indicates potential applications of the designed indentation device for *in situ* studies regarding mechanically-induced transformation processes in general.

B. Modifications of the crystal structure of high density polyethylene films

Accounting for about 40% of the total volume of world production of plastic materials,[50] polyethylene is not only an important commercial polymer but also often used as a model system due to its chemical simplicity.[51,52] The PE crystal exhibits an orthorhombic structure whereby the carbon skeleton of the polymer chains has a planar zigzag structure. Each atom of the carbon backbone forms with two hydrogen atoms a methylene (CH_2) group. The application of pressure leads to well characterized changes in the vibrational modes associated with the strained PE chain components. Studies on the pressure dependent properties of polymers provide insights into the fundamental molecular interactions that dictate the performance of polymer components under high-pressure conditions observed in industrial applications, such as friction in bearings, pressure molding, and structural reinforcement.[53,54]

To validate the capability of the instrument to measure Raman frequency shifts on polymer samples, a biaxially oriented, high density PE (HDPE) film was indented. The 50 μm thick film sample was glued to a sapphire window using cyanoacrylate glue (Super Glue, Rancho Cucamonga, CA).[33] The film was indented using a sapphire flat punch truncated cone (nominal diameter 50 μm) using a series of loading steps; a Raman spectrum was collected at each step from the deformed contact region underneath the indenter. The main change in the Raman spectrum of PE was observed in the frequency region between 1410 cm^{-1} and 1465 cm^{-1}. The three peaks with center frequencies at 1415 cm^{-1}, 1439 cm^{-1}, and 1461 cm^{-1} located in this region are associated with vibrations of the angle of the methylene group (CH_2 bend mode).[25,50,52,53,56–58] With increasing contact pressure, the three-peak features merge into one broad peak (Fig. 5(b)). Due to changes in the intensities and shifts in the center frequencies of the different peaks.[50,53,55,56] Alterations in the bend mode region similar to those observed in this study have been correlated with increased disorder (amorphization) of the PE structure.[24,59] However, the mechanically induced changes in the PE structure are reversible as the distinct three-peak feature is restored during release of the compressive pressure on the sample. This was expected as the contact pressure is below the transition pressure of 2.5 GPa, above which changes in the molecular structure remain permanent.[56]

The results clearly demonstrate the capability of the *in situ* indenter to collect spectroscopic information on pressure induced crystal deformations in (semi-)crystalline polymers.

V. CONCLUSION AND FUTURE DEVELOPMENTS

This paper describes the design, calibration, and operation of an indentation device that is coupled with a Raman

microscope to conduct *in situ* spectroscopic and optical analysis of mechanically deformed regions of Raman-active, transparent bulk materials, thin films or fibers under contact loading. The performance of the designed experimental set-up was compared to commercial instruments and its capabilities were demonstrated in two example studies, thereby, showing the usefulness of this instrument in advancing the understanding of deformation behavior of materials in complex stress conditions.

Currently, the experimental setup only allows the collection of Raman spectra from individual spatial locations on the specimen of interest, a configuration referred to as a Raman microprobe. A planned further refinement of the instrument would allow collection of Raman spectra over an entire image (Raman mapping). This collection of spectra could then be analyzed to yield spatial maps of material quantities that can be extracted from the Raman spectra including strain, crystalline alignment, phase, or composition. This would give the opportunity for *in situ* studies of the stress fields around indentations or crack tips and be extremely helpful in evaluating and refining existing theoretical models in this field.

[1] A. Gouldstone, N. Chollacoop, M. Dao, J. Li, A. A. Minor, and Y.-L. Shen, Acta Mater. **55**, 4015 (2007).
[2] *Handbook of Nanoindentation with Biological Applications*, edited by M. L. Oyen (Pan Stanford, Singapore, 2010)
[3] C. A. Schuh, Mater. Today **9**, 32 (2006).
[4] D. B. Marshall and B. R. Lawn, J. Mater. Sci. **14**, 2001 (1979).
[5] B. R. Lawn, T. P. Dabbs, and C. J. Fairbanks, J. Mater. Sci. **18**, 2785 (1983).
[6] R. F. Cook and G. M. Pharr, J. Am. Ceram. Soc. **73**, 787 (1990).
[7] R. Tandon, D. J. Green, and R. F. Cook, J. Am. Ceram. Soc. **73**, 2619 (1990).
[8] R. F. Cook and E. G. Liniger, J. Am. Ceram. Soc. **76**, 1096 (1993).
[9] J. Thurn, D. J. Morris, and R. F. Cook, J. Mater. Res. **17**, 2679 (2002).
[10] D. J. Morris and R. F. Cook, J. Am. Ceram. Soc. **87**, 1494 (2004).
[11] D. F. Bahr and W. W. Gerberich, J. Mater. Res. **13**, 1065 (1998).
[12] R. Rabe, J.-M. Breguet, P. Schwaller, S. Stauss, F.-J. Haug, J. Patscheider, and J. Michler, Thin Solid Films **469–470**, 206 (2004).
[13] E. A. Stach, T. Freeman, A. A. Minor, D. K. Owen, J. Cumings, M. A. Wall, T. Chraska, R. Hull, J. W. Morris, Jr., A. Zettl, and U. Dahmen, Microsc. Microanal. **7**, 507 (2001).
[14] M. S. Bobji, C. S. Ramanujan, J. B. Pethica, and B. J. Inkson, Meas. Sci. Technol. **17**, 1324 (2006).
[15] A. Gourrier, M. C. Garcia Gutiérrez, and C. Riekel, Macromolecules **35**, 8072 (2002).
[16] I. V. Gridneva, Y. V. Milman, and V. I. Trefilov, Phys. Status Solidi **14**, 77 (1972).
[17] D. R. Clarke, M. C. Kroll, P. D. Kirchner, R. F. Cook, and B. J. Hockey, Phys. Rev. Lett. **60**, 2156 (1988).
[18] G. M. Pharr, W. C. Oliver, R. F. Cook, P. D. Kirchner, M. C. Kroll, T. R. Dinger, and D. R. Clarke, J. Mater. Res. **7**, 961 (1992).
[19] J. E. Bradby, J. S. Williams, and M. V. Swain, Phys. Rev. B **67**, 085205 (2003).
[20] T. Jochum, I. E. Reimanis, M. J. Lance, and E. R. Fuller, Jr., J. Am. Ceram. Soc. **92**, 857 (2009).
[21] Y. Gogotsi, T. Miletich, M. Gardner, and M. Rosenberg, Rev. Sci. Instrum. **70**, 4612 (1999).
[22] V. Domnich and Y. Gogotsi, Rev. Adv. Mater. Sci. **3**, 1 (2002).
[23] A. M. Bolon and M. M. Gentleman, J. Am. Ceram. Soc. **94**, 4478 (2001).
[24] G. R. Strobl and W. Hagedorn, J. Polym. Sci., Polym. Phys. Ed. **16**, 1181 (1978).
[25] M. Pigeon, R. E. Prud'homme, and M. Pézolet, Macromolecules **24**, 5687 (1991).
[26] M. J. Gall, P. J. Hendra, C. J. Peacock, M. E. A. Cudby, and H. A. Willis, Spectrochim. Acta **28 A**, 1485 (1972).
[27] P. J. Hendra, H. P. Jobic, E. P. Marsden, and D. Bloor, Spectrochim. Acta, Part A **33**, 1316 (1977).
[28] N. Muraki, G. Katagiri, V. Sergo, G. Pezzotti, and T. Nishida, J. Mater. Sci. **32**, 5419 (1997).
[29] G. Gouadec and P. Coloman, Mater. Sci. Eng., A **288**, 132 (2000).
[30] Y. B. Gerbig, S. Stranick, and R. F. Cook, Scr. Mater. **63**, 512 (2010).
[31] T. Wermelinger and R. Spolenak, J. Appl. Phys. **106**, 064907 (2009).
[32] P. Puech, F. Demangeot, J. Frandon, C. Pinquier, M. Kuball, V. Domnich, and Y. Gogotsi, J. Appl. Phys. **96**, 2853 (2004).
[33] Any mention of commercial products within this paper is for information only; it does not imply recommendation or endorsement by NIST.
[34] J. J. Parise, L. L. Howell, and S. P. Magleby, Mech. Mach. Theory **36**, 1281 (2001).
[35] B. N. Taylo and C. E. Kuyatt, *Guidelines for Evaluating and Expressing the Uncertainty of NIST Measurements Results* NIST Technical Note 1297, Department of Commerce, Gaithersburg, MD, 1994.
[36] W. C. Oliver and G. M. Pharr, J. Mater. Res. **7**, 1564 (1992).
[37] A. Mujica, A. Rubio, A. Munoz, and R. J. Needs, Rev. Mod. Phys. **75**, 863 (2003).
[38] G. M. Pharr, W. C. Oliver, and D. S. Harding, J. Mater. Res. **6**, 1129 (1991).
[39] R. Rao, J. E. Bradby, and J. S. Williams, Appl. Phys. Lett. **91**, 123113 (2007).
[40] B. D. Malone, J. D. Sau, and M. L. Cohen, Phys. Rev. B **87**, 161202(R) (2008).
[41] P. Eyben, F. Clemente, K. Vanstreels, G. Purtois, T. Clarysse, K. Sankaran, J. Mody, W. Vandervorst, K. Mylvaganam, and L. Zhang, J. Vac. Sci. Technol. B **28**, 401 (2010).
[42] D. E. Kim and S. I. Oh, J. Appl. Phys. **104**, 013502 (2008).
[43] Y.-H. Lin, S.-R Jian, Y.-S. Lai, and P.-F. Yang, Nanoscale Res. Lett. **2**, 71 (2008).
[44] C. F. Sanz-Navarro, S. D. Kenny, and R. Smith, Nanotechnology **15**, 692 (2004).
[45] G. S. Smith, E. B. Tadmor, N. Bernstein, and E. Kaxiras, Acta Mater. **49**, 4089 (2001).
[46] L. L. Boyer, E. Kaxiras, J. L. Feldman, J. Q. Broughton, and M. J. Mehl, Phys. Rev. Lett. **67**, 715 (1991).
[47] K. Mylvaganam, L. C. Zhang, P. Eyben, J. Mody, and W. Vandervorst, Nanotechnology **20**, 305705 (2009).
[48] S. Ruffell, J. E. Bradby, J. S. Williams, R. C. Major, and O. L. Warren, Mater. Res. **1146**, 1146-NNO2-06 (2009).
[49] Y. B. Gerbig, C. A. Michaels, A. M. Forster, and R. F. Cook, Phys. Rev. B **85**, 104102 (2012).
[50] L. Fontana, M. Santoro, R. Bini, D. Q. Vinh, and S. Scandolo, J. Chem. Phys. **133**, 204502 (2010).
[51] J. Barnes and B. Fanconi, J. Phys. Chem. Ref. Data **7**, 1309 (1978).
[52] S. A. Gordeyev, G. Y. Nikolaeva, and K. A. Prokhorov, Laser Phys. **6**, 121 (1996).
[53] D. J. Lacks, J. Phys. Chem. **99**, 14430 (1995).
[54] G. A. Pfeffer and D. W. Noid, Macromolecules **23**, 2573 (1990).
[55] W. W. Ley and H. G. Drickamer, J. Phys. Chem. **93**, 7262 (1989).
[56] Y. Zhao, J. Wang, Q. Cui, Z. Liu, M. Yang, and J. Shen, Polymer **31**, 1425 (1990).
[57] S. Krimm, C. Y. Liang, and G. B. B. M. Sutherland, J. Chem. Phys. **25**, 549 (1956).
[58] H. Sato, M. Shimoyama, T. Kamiya, T. Amari, S. Sasic, T. Ninomiya, H. W. Siesler, and Y. Ozaki, J. Appl. Polym. Sci. **86**, 443 (2002).
[59] R. P. Paradkar, S. S. Sakhalkar, X. He, and M. S. Ellison, J. Appl. Polym. Sci. **88**, 545 (2003).